Aleni, Afshin Hasani; Kretzschmar, Niklas; Jansson, Anton; Ituarte, Iñigo Flores; St-Pierre, Luc

3D printing of dense and porous TiO_2 structures

Published in:
Ceramics International

DOI:
10.1016/j.ceramint.2020.03.248

Published: 01/07/2020

Document Version
Peer-reviewed accepted author manuscript, also known as Final accepted manuscript or Post-print

3D printing of dense and porous TiO_2 structures

Afshin Hasani Aleni[1], Niklas Kretzschmar[1], Anton Jansson[2], Iñigo Flores Ituarte [3], Luc St-Pierre[1]

1 Department of Mechanical Engineering, Aalto University, Espoo, Finland

2 Department of Mechanical Engineering, Orebro University, Orebro, Sweden

3 Department of Materials and Production, Aalborg University, Copenhagen, Denmark

Abstract

Direct foam writing allows the fabrication of highly porous and hierarchical ceramic structures with high specific mechanical properties. This manufacturing technique, however, has mainly used stabilized Al_2O_3 foam inks. In this work, we present a novel foam ink based on TiO_2. This ink uses polyvinyl alcohol (PVA) as a binder and a small amount of zinc as a frothing agent. We used this ink to produce cylindrical foam samples via direct foam writing. The foams had a porosity of up to 65% and a mean pore size of 180 μm, which is significantly larger than previously reported for direct foam writing with Al_2O_3. The foams were tested in compression and were found to have an elastic modulus of 0.5 GPa and a compressive strength of 12-18 MPa. These mechanical properties are similar to those of porous ceramics produced by conventional manufacturing routes. Therefore, this work represents a step forward by broadening the direct foam writing process to a wider range of porous ceramics.

Keywords: Titanium dioxide (TiO_2); Foam; Additive manufacturing; Robocasting ceramics; Direct foam writing.

1 Introduction

Ceramic foams are used in a wide range of engineering applications including filtration, thermal insulation, catalyst supports, tissue scaffolding, implants and lightweight structures [1-4]. Their properties are governed by their pore size, type and distribution, and different manufacturing routes have been developed to control these microstructural characteristics. Conventional manufacturing techniques can be classified in three categories: (i) polymer/wood replica, (ii) sacrificial templating, and (iii) direct foaming [5,6].

The replica technique consists of impregnating a polymer foam or wood with a ceramic suspension, and then removing the polymer/wood template. This process often leads to damaged cell walls, which decreases the strength of the foam [6]. This inconvenience can be avoided with sacrificial templating. With this process, a sacrificial phase is incorporated to the ceramic suspension which is later evaporated during the sintering process to create pores. This produces stronger foams, but the process can generate a large amount of waste gases [6]. This issue can be circumvented with direct foaming. This technique consists of incorporating air into a ceramic suspension and relies on particles or surfactants to stabilize the wet foam. This process offers a fast and inexpensive way to produce ceramic foams with a wide range of porosities and pore sizes.

Another advantage of direct foaming is that the ceramic foam suspension can be used as an ink for robocasting. Robocasting, also known as direct ink writing, is an additive manufacturing technique in which ink is extruded through a nozzle to build a structure layer-by-layer [7–9]. Ceramic parts can be produced with this process using either a dense ink [10–13] or a foam ink, which is known as direct foam writing [14–17]. Direct foam writing is not the only additive manufacturing technique suitable for producing ceramic foams; these can also be made by selective laser sintering of hollow microspheres [18–20]. Otherwise, dense ceramic parts can be produced by many different additive manufacturing techniques, such as stereolithography [21–23] and selective laser sintering/melting [24–28]. For more details on additive manufacturing of ceramics, see the review of Chen et al. [9].

In this article, we focus on direct ink/foam writing because this technique is fast, inexpensive, and suitable to produce large ceramic components. Another advantage of direct foam writing is the possibility to create hierarchical cellular structures: scaffolds or honeycombs where the

cell walls are porous [14-17]. The hierarchical structures have an ultrahigh overall porosity and a high specific stiffness and strength. One limitation, however, is that most studies have used an alumina (Al_2O_3) foam ink; hence, there is a need to explore if direct foam writing can be used with other types of ceramic.

Titanium dioxide (TiO_2) has attracted research interest because of its photocatalytic activity, but its high bioactivity and biocompatibility also make it an attractive material for implants [29–33]. Therefore, this paper aims to assess the potential of TiO_2 for direct ink/foam writing. We present a method to prepare (i) dense and (ii) foam TiO_2 inks that is simple, low-cost, and does not require stabilizers.

The paper is organized as follows. The preparation of the dense and foam inks is detailed in Section 2, along with the methodology used to prepare samples by robocasting. The morphology of the specimens and their compressive responses are presented in Section 3. Finally, the porosity, pore size and mechanical properties of our foams are compared to those of other ceramic foams reported in the literature.

2 Material and methods

2.1 Sample preparation

Both dense and foam samples were prepared by additive manufacturing in three steps. First, the ink necessary to print the samples was prepared. Second, the ink was loaded in a universal extrusion machine to print the samples layer-by-layer. Third, the specimens were sintered to reach their full mechanical properties. Each step is detailed below.

2.1.1 Ink preparation

The ink used to produce the dense sample was prepared by combining 80 wt% of commercially available TiO2 powder (45 μm particle size, rutile, high purity 95%) with 20 wt% of polyvinyl alcohol (PVA 2%, pH~5-6 diluted acid), which acted as a binder [34–37]. The powder and binder were blended into a homogenous mixture using a high-speed mixer for 8 min, starting at 1200 rpm and increasing the speed by 100 rpm every 2 min up to 1500 rpm.

On the other hand, the foam ink was made by adding 5 wt% of pure zinc (Zn) powder (liquid density of 6.57 g/cm3 and boiling point of 907°C) into 45 wt% of PVA 2%. The chemical reaction between zinc and PVA releases hydrogen bubbles transforming the mixture into a foam. The process, however, is slow so to accelerate it, the solution was mixed while the reaction took place (1 min at 1200, 1300, and 1400 rpm and 10 min at 1500 rpm). Next, 45 wt% of TiO2 powder was added and mixed in four increments at 1300 rpm. In the first three increments, 10 wt% of TiO2 powder was added and mixed for 1 min, whereas for the last increment, 15 wt% was added and mixed for 7 min. Finally, 5 wt% of rice flour was added and mixed for 5 min at 1500 rpm to strengthen the foam ink and delay drying [16,38–40]. The rheological properties of dense and foam inks were characterized at room temperature (22°C), two hours after preparation. Measurements were done using a Physica MCR 301 rheometer with a plate-plate geometry of 20 mm in diameter. The ink viscosity is plotted as a function of shear rate in Fig. 1. As expected, the viscosity of the foam ink is significantly less than that of the dense ink. The viscosity of the foam ink is similar to that measured by Muth et al. [16] for direct foaming of alumina powder.

2.1.2 Printing process and drying

All samples were printed layer-by-layer with a universal extrusion machine. The dense or foam ink was loaded into a 12 ml syringe equipped with a plastic nozzle of 0.84 mm in diameter. All green bodies printed had a cylindrical shape of diameter D = 12.7 mm and height H = 25.4 mm. The digital print path was drawn by Solidworks and converted to G-Code commands by PranterFace software. The printing flow speed was critical to the process and had to be adjusted depending on the type of specimen. Dense samples were printed with a flow speed of 0.024 mm/s, whereas foams required a slower extrusion rate of 0.010 mm/s. All samples were printed on a glass plate; however, for foams, the glass plate was covered by a thin layer (0.5 mm) of petroleum jelly to ensure that the samples maintained their cylindrical shape when drying (shrinkage at the base is less than that at the top of the specimen without petroleum jelly).

After printing, dense specimens were left to dry at room temperature for a week. In contrast, foam samples were placed in a box along with thick wet sponges to control humidity. After

spending a week in the box, the foam structures were taken out and dried at room temperature for an additional three days before sintering. This slow drying process is very similar to that used in other studies [16,17] and, in our experience, reducing the drying process to 24, 48 or 72h led to the formation of cracks during sintering.

2.1.3 Sintering

Both dense and foam green bodies were sintered at 1300°C for 1 h; however, the two types of samples followed different temperature profiles. For dense samples, the temperature was increased at a rate of 2°C/min up to 500°C. After spending 1 h at 500°C, the temperature was increased up to 1300°C at a rate of 5°C/min.

The temperature profile used for foams was significantly less steep to avoid gas bubbles bursting during the process. The profile included five isothermal stages of 1 h at 60, 120, 240 and 500°C. The first two increases in temperature were done at a rate of 0.5°C/min; the next two used 1°C/min; then, 2°C/min; and finally, 3°C/min. After being sintered for 1 h at 1300°C, both dense and foam samples were cooled down at a rate of 2°C/min. Note that the sintering process is expected to remove the PVA binder, which evaporates at 500°C, and, in the case of foams, the zinc, which has a boiling point around 950-1100°C.

2.1.4 Dimensions and shrinkage

The dimensions of each sample were measured after printing[*], drying, and sintering to quantify shrinkage. The diameter D and height H were measured with calipers and are listed in Table 1. All samples had similar dimensions after printing, and these were close to the dimensions of the CAD model (D = 12.7 mm and H = 25.4 mm). Measurements taken after drying and after sintering showed that the foams shrunk significantly more than dense samples. Shrinkage was similar in both radial and longitudinal directions, see Table 1. Dense specimens shrunk by about 25%, of which only 5% occurred during the drying process. In contrast, foams shrunk by 41-50% and almost half of this occurred while the green bodies were drying.

[*] The dimensions referred here as 'after printing' were in fact measured three days after printing. The sample were too wet and soft to be measured earlier without risking to damage them.

Photographs of dense and foam samples, taken before and after sintering, are shown in Fig. 2. Clearly, the foam is significantly smaller than the dense specimen as a consequence of the shrinkage reported above. All samples have a clear layer-by-layer construction due to the printing process, and this structure is present before and after sintering.

Finally, the density of each sample is reported in Table 2. To evaluate the density, the mass was measured with a scale, whereas the volume was estimated as follows. First, a photograph of the sample, such as Fig. 2, was imported into the commercial software Solidworks using the sketch picture option. Second, a polyline was drawn along the irregular left edge of the sample with high accuracy and the axis of revolution was identified from the photograph. Third, the polyline was rotated about the axis of revolution to create a 3D solid, and its volume was calculated automatically by Solidworks. Repeating this procedure with another photograph (or by tracing the right edge of the sample) gave a slightly different volume, but repeatability tests indicated that the measurements were within 5%.

Dense samples had a density around 3.6 g/cm^3, which is about 10% less than the density of pure titanium dioxide (3.970 g/cm^3) reported in [41]. In contrast, foams had a density between 1.030 and 1.220 g/cm^3, about three times lower than dense samples.

2.2 Characterization

2.2.1 Elemental analysis and phase identification

Energy Dispersive X-ray (EDX) spectroscopy was used to determine the elemental composition of the samples. For this analysis, the samples were coated with a 4 nm layer of gold and placed in a scanning electron microscope (JEOL JSM-7500FA). In addition, X-ray Diffraction (XRD) was carried out for phase identification. For XRD, the sample was ground to fine powder and placed on a standard glass sample holder. The XRD scan (2θ symmetric reflection) was performed using a Rigaku SmartLab 9 kW multipurpose diffractometer using Cu $K_{\alpha 1}$ radiation with a wavelength of 1.54 Å. The measured 2θ range was from 15-100°. Preliminary fast scans from 5-100° were carried out to identify the relevant scanning range.

2.2.2 Computed tomography

All samples were scanned in the SkyScan 1272 computed tomography (CT) system to quantify their porosity. In all cases, the acceleration voltage was set to 100 kV and the

filament current was 100 μA. A 0.11 mm copper filter was applied to the spectrum to reduce the beam hardening artefact (a standard procedure in CT). Dense samples were scanned with a voxel size of approximately 1 μm^3, whereas a larger resolution of 3 μm^3 was used for foams. Each sample took roughly 30 h to scan, and the images were collected using the software VGstudioMax 3.0.

The porosity of each specimen was evaluated using the built-in function in VGstudioMax 3.0. The volume used for this analysis was roughly 15 mm^3 for dense samples, and approximately 130 mm^3 for foams. Subsequently, CT scan images were imported to the software ImageJ, which was used to measure the average pore size of the foams.

2.2.2 Compression tests

All samples were tested in compression using an Instron 33R testing machine. The cross-head speed was set to 5 mm/min, corresponding to a strain rate of approximately 0.004 s^{-1}. The compressive force was measured by a load cell with a capacity of 100 kN.

3 Results

3.1.1 Elemental analysis and phase identification

The results of the EDX analysis are presented in Fig. 3a for dense samples and in Fig. 3b for foams. In both cases, the samples are made of titanium and oxygen (with a small amount of gold, which was used as a coating for the SEM). The EDX analysis indicated that both the PVA binder and the zinc frothing agent used for foams evaporated during the sintering process. The XRD analysis of dense and foam samples is given in Fig.3c and d, respectively. Clearly, the rutile phase of TiO_2 was predominant in both samples.

3.2 Morphological characterization

Images from the CT scans are shown in Fig. 4 for both dense and foam samples. For each sample, two perpendicular cross-sections are shown: the circular images are cross-sections perpendicular to the longitudinal axis of the sample, whereas the rectangular images are perpendicular to the radial axis of the specimen.

The CT images of dense samples revealed the presence of fairly large voids with a diameter of 200-300 μm. Smaller voids (about 50 μm in diameter) were also present, and it seemed that dense sample 3 (Fig. 4c) contained a higher concentration of voids than the other two dense samples. Further images of all three dense samples (Fig. 5) confirmed this: sample 3 contained a much higher concentration of small voids than the other samples and the largest pores were found in dense sample 2 (Fig. 5b).

The porosity of dense samples varied from 8.6 to 17.6%, and the value for each specimen is given in Table 2. This fairly high and variable porosity is likely to be due to be the presence of air bubbles in the ink used for the printing process.

In contrast, foams had a porosity between 55 and 65%, see Table 2. Images of the foams showed that their pores were equiaxed and uniformly distributed, see Fig. 4 d-f. The frequency distribution of the pore size is given in Fig. 6 for each sample. Overall, the pore size varied from 40-650 μm, and the average pore size was 180 μm.

3.3 Mechanical properties

The compressive responses of both dense and foam samples were measured up to failure, and the stress versus strain curves are plotted in Fig. 7. In general, all specimens had a linear elastic behavior up to fracture. Some responses (see, for example, dense sample 2) exhibited small load drops due to fragments breaking off the sample. The elastic modulus and ultimate compressive strength measured are summarized in Table 2 for each sample.

The dense specimens had an elastic modulus around 5 GPa and a compressive strength of approximately 100 MPa. These mechanical properties are significantly below those measured for the same material produced by conventional manufacturing techniques (for example, Li et al. [42] measured an elastic modulus of 270 GPa and a three-point bending strength of 426 MPa). We think that the porosity and the large voids present in dense samples (see Fig. 4 and 5) explain why the properties measured here are lower than those obtained by conventional manufacturing techniques.

On the other hand, foams had an elastic modulus of 0.5 GPa and a compressive strength varying from 12-18 MPa, see Table 2. These variations in strength were correlated to the

porosity of the foam; strength increased with decreasing porosity. Overall, the density of foams was about 30% of that of dense samples, whereas their elastic modulus and strength was about 10% of those measured for their dense counterparts.

3.4 Comparison with other ceramic foams

In this section, we compare the morphology and mechanical properties of our foam samples to those of other ceramic foams reported in the literature. First, the porosity and average pore size are compared in Fig. 8. The data include foams produced by direct foam writing and via conventional manufacturing routes (such as polymer/wood replica, sacrificial templating and direct foaming with particles or surfactants).

Clearly, the porosity and average pore size obtained in this study are in the middle of the range covered by conventional manufacturing techniques, see Fig. 8. When comparing samples produced by direct foam writing only, we can see that our specimens have a much larger pore size. Such a striking difference can be attributed to the fact that other studies used a much finer powder to prepare their foam ink; for example, Muth et al.[16] used an alumina powder with a mean particle size of 0.3 μm, whereas we used titanium dioxide powder with a particle size of 45 μm. This tends to indicate that the zinc foaming technique makes it possible to prepare foam inks with a relatively coarse powder. This could be advantageous for producing low-cost ceramic foams since the price of powder is inversely proportional to its mean particle size. Overall, the results in Fig. 8 demonstrate that direct foam writing has the potential to produce foams with a wide range of pore size; however, more studies are needed to correlate the pore size of the foam to the mean particle size of the powder.

Next, the mechanical properties of our samples are compared to those of other ceramic foams in Fig. 9. Data on TiO_2 foams are limited; therefore, we compared our results to those obtained for Al_2O_3 foams. This is a fair comparison since both these dense ceramics have a similar elastic modulus E_s = 280 GPa [41] and a three-point bending strength σ_s = 400 MPa [6]. The elastic modulus E, normalized by E_s = 280 GPa, is plotted in Fig. 9a, whereas the compressive strength σ, normalized by σ_s = 400 MPa, is shown in Fig. 9b. Both quantities

are plotted as a function of the relative density, which is defined as the complement of the porosity. Note that many studies on porous ceramics report the compressive strength, but not the elastic modulus. Consequently, Fig. 9b includes significantly more data than Fig. 9a.

The results in Fig. 9a indicate that our foams have a significantly lower elastic modulus than those prepared by Muth et al. [16]. This could be due to two factors. First, Muth et al. [16] sintered their foams at 1500°C, whereas we used a lower temperature of 1300°C. Second, the finer powder used by Muth et al. [16] may reduce the number and size of defects, leading to higher mechanical properties. Nonetheless, our samples have an elastic modulus comparable to that of foams manufactured by conventional routes.

Next, we turn our attention to the compressive strength compared in Fig. 9b. Our samples have a compressive strength almost equal to that measured by Ren et al. [17], who also used direct foam writing to produce their specimens. In addition, our samples have a similar strength to those of foams produced by conventional manufacturing routes: our specimens outperform those prepared using polymer or wood replicas, and their strength is comparable to foams obtained by sacrificial templating.

4 Conclusion

Dense and foam inks were developed to produce ceramic structures via direct ink writing. The dense ink was prepared by combining TiO_2 powder with PVA. This mixture was turned into a foam ink with the addition of zinc, which reacted with the PVA to create bubbles. This new zinc foaming technique allowed us to prepare a foam ink using much coarser ceramic powder than previously reported in [14–16]. The foams had a porosity up to 65% and an average pore size of 180 μm, which is nearly an order of magnitude larger than previously reported for direct foam writing [14–16]. Finally, compression tests revealed that the foams had an elastic modulus and a compressive strength comparable to those obtained by conventional manufacturing techniques, such as direct foaming, sacrificial templating and polymer/wood replica.

References

[1] M.A.A. Mendes, P. Goetze, P. Talukdar, E. Werzner, C. Demuth, P. Rössger, R. Wulf, U. Gross, D. Trimis, S. Ray, Measurement and simplified numerical prediction of effective thermal conductivity of open-cell ceramic foams at high temperature, Int. J. Heat Mass Transf. 102 (2016) 396–406. https://doi.org/10.1016/j.ijheatmasstransfer.2016.06.022.

[2] P. Kumar, F. Topin, The geometric and thermohydraulic characterization of ceramic foams: An analytical approach, Acta Mater. 75 (2014) 273–286. https://doi.org/10.1016/j.actamat.2014.04.061.

[3] S. Barg, C. Soltmann, M. Andrade, D. Koch, G. Grathwohl, Cellular ceramics by direct foaming of emulsified ceramic powder suspensions, J. Am. Ceram. Soc. 91 (2008) 2823–2829. https://doi.org/10.1111/j.1551-2916.2008.02553.x.

[4] F. Luthardt, J. Adler, A. Michaelis, Characteristics of a Continuous Direct Foaming Technique, Int. J. Appl. Ceram. Technol. 12 (2015) E133–E138. https://doi.org/10.1111/ijac.12376.

[5] T. Ohji, M. Fukushima, Macro-porous ceramics: processing and properties, Int. Mater. Rev. 57 (2012) 115–131. https://doi.org/10.1179/1743280411Y.0000000006.

[6] R. Studart, U.T. Gonzenbach, E. Tervoort, L.J. Gauckler, Processing Routes to Macroporous Ceramics: A Review, 89 (2006) 1771–1789. https://doi.org/10.1111/j.1551-2916.2006.01044.x.

[7] J.A. Lewis, J.E. Smay, J. Stuecker, J. Cesarano, Direct ink writing of three-dimensional ceramic structures, J. Am. Ceram. Soc. 89 (2006) 3599–3609. https://doi.org/10.1111/j.1551-2916.2006.01382.x.

[8] A. Zocca, P. Colombo, C.M. Gomes, J. Günster, Additive Manufacturing of Ceramics: Issues, Potentialities, and Opportunities, J. Am. Ceram. Soc. 98 (2015) 1983–2001. https://doi.org/10.1111/jace.13700.

[9] Z. Chen, Z. Li, J. Li, C. Liu, C. Lao, Y. Fu, C. Liu, Y. Li, P. Wang, Y. He, 3D printing of ceramics: A review, J. Eur. Ceram. Soc. 39 (2019) 661–687.

https://doi.org/10.1016/j.jeurceramsoc.2018.11.013.

[10] A.H. Aleni, I.F. Ituarte, A. Mohite, L. St-Pierre, J. Partanen, Comparing stiffness of solid and scaffold nano-TiO2 structures produced by material extrusion method, Ceram. Int. 44 (2018) 2231–2239. https://doi.org/10.1016/j.ceramint.2017.10.181.

[11] L. Rueschhoff, W. Costakis, M. Michie, J. Youngblood, R. Trice, Additive Manufacturing of Dense Ceramic Parts via Direct Ink Writing of Aqueous Alumina Suspensions, Int. J. Appl. Ceram. Technol. 13 (2016) 821–830. https://doi.org/10.1111/ijac.12557.

[12] C.F. Revelo, H.A. Colorado, 3D printing of kaolinite clay ceramics using the Direct Ink Writing (DIW) technique, Ceram. Int. 44 (2018) 5673–5682. https://doi.org/10.1016/j.ceramint.2017.12.219.

[13] G. Franchin, L. Wahl, P. Colombo, Direct ink writing of ceramic matrix composite structures, J. Am. Ceram. Soc. 100 (2017) 4397–4401. https://doi.org/10.1111/jace.15045.

[14] C. Minas, D. Carnelli, E. Tervoort, A.R. Studart, 3D Printing of Emulsions and Foams into Hierarchical Porous Ceramics, Adv. Mater. 28 (2016) 9993–9999. https://doi.org/10.1002/adma.201603390.

[15] J. Maurath, N. Willenbacher, 3D printing of open-porous cellular ceramics with high specific strength, J. Eur. Ceram. Soc. 37 (2017) 4833–4842. https://doi.org/10.1016/j.jeurceramsoc.2017.06.001.

[16] J.T. Muth, P.G. Dixon, L. Woish, L.J. Gibson, J.A. Lewis, Architected cellular ceramics with tailored stiffness via direct foam writing, Proc. Natl. Acad. Sci. (2017). https://doi.org/10.1073/pnas.1616769114.

[17] B. Ren, J. Liu, Y. Wang, Y. Chen, K. Gan, Y. Rong, J. Yang, Hierarchical cellular scaffolds fabricated via direct foam writing using gelled colloidal particle-stabilized foams as the ink, J. Am. Ceram. Soc. (2019) 1–9. https://doi.org/10.1111/jace.16543.

[18] A.N. Chen, M. Li, J. Xu, C.H. Lou, J.M. Wu, L.J. Cheng, Y.S. Shi, C.H. Li, High-

porosity mullite ceramic foams prepared by selective laser sintering using fly ash hollow spheres as raw materials, J. Eur. Ceram. Soc. 38 (2018) 4553–4559. https://doi.org/10.1016/j.jeurceramsoc.2018.05.031.

[19] S.S. Liu, M. Li, J.M. Wu, A.N. Chen, Y.S. Shi, C.H. Li, Preparation of high-porosity Al2O3 ceramic foams via selective laser sintering of Al2O3 poly-hollow microspheres, Ceram. Int. 46 (2020) 4240–4247. https://doi.org/10.1016/j.ceramint.2019.10.144.

[20] M. Li, A.N. Chen, X. Lin, J.M. Wu, S. Chen, L.J. Cheng, Y. Chen, S.F. Wen, C.H. Li, Y.S. Shi, Lightweight mullite ceramics with controlled porosity and enhanced properties prepared by SLS using mechanical mixed FAHSs/polyamide12 composites, Ceram. Int. 45 (2019) 20803–20809. https://doi.org/10.1016/j.ceramint.2019.07.067.

[21] R. He, G. Ding, K. Zhang, Y. Li, D. Fang, Fabrication of SiC ceramic architectures using stereolithography combined with precursor infiltration and pyrolysis, Ceram. Int. 45 (2019) 14006–14014. https://doi.org/10.1016/j.ceramint.2019.04.100.

[22] F. Scalera, C. Esposito Corcione, F. Montagna, A. Sannino, A. Maffezzoli, Development and characterization of UV curable epoxy/hydroxyapatite suspensions for stereolithography applied to bone tissue engineering, Ceram. Int. 40 (2014) 15455–15462. https://doi.org/10.1016/j.ceramint.2014.06.117.

[23] A.J.J. Zak C. Eckel, Chaoyin Zhou, John H. Martin, T.A.S. William B. Carter, Additive manufacturing of polymer-derived ceramics, 351 (2016) 3–8.

[24] K. Shahzad, J. Deckers, S. Boury, B. Neirinck, J.P. Kruth, J. Vleugels, Preparation and indirect selective laser sintering of alumina/PA microspheres, Ceram. Int. 38 (2012) 1241–1247. https://doi.org/10.1016/j.ceramint.2011.08.055.

[25] K. Shahzad, J. Deckers, Z. Zhang, J.P. Kruth, J. Vleugels, Additive manufacturing of zirconia parts by indirect selective laser sintering, J. Eur. Ceram. Soc. 34 (2014) 81–89. https://doi.org/10.1016/j.jeurceramsoc.2013.07.023.

[26] T. Friedel, N. Travitzky, F. Niebling, M. Scheffler, P. Greil, Fabrication of polymer derived ceramic parts by selective laser curing, J. Eur. Ceram. Soc. 25 (2005) 193–

197. https://doi.org/10.1016/j.jeurceramsoc.2004.07.017.

[27] Y. Li, Y. Hu, W. Cong, L. Zhi, Z. Guo, Additive manufacturing of alumina using laser engineered net shaping: Effects of deposition variables, Ceram. Int. 43 (2017) 7768–7775. https://doi.org/10.1016/j.ceramint.2017.03.085.

[28] X. Tian, J. Günster, J. Melcher, D. Li, J.G. Heinrich, Process parameters analysis of direct laser sintering and post treatment of porcelain components using Taguchi's method, J. Eur. Ceram. Soc. 29 (2009) 1903–1915. https://doi.org/10.1016/j.jeurceramsoc.2008.12.002.

[29] L. Chen, C. Huang, G. Xu, S.L. Hutton, L. Miao, Macroporous TiO2 foam with mesoporous walls, Mater. Charact. 75 (1970) 8–12. https://doi.org/10.1016/j.matchar.2012.09.010.

[30] N. Drnovšek, K. Rade, R. Milačič, J. Štrancar, S. Novak, The properties of bioactive TiO2 coatings on Ti-based implants, Surf. Coatings Technol. 209 (2012) 177–183. https://doi.org/10.1016/j.surfcoat.2012.08.037.

[31] F. López-Huerta, B. Cervantes, O. González, J. Hernández-Torres, L. García-González, R. Vega, A.L. Herrera-May, E. Soto, Biocompatibility and surface properties of TiO2 thin films deposited by DC magnetron sputtering, Materials (Basel). 7 (2014) 4105–4117. https://doi.org/10.3390/ma7064105.

[32] I. Ali, M. Suhail, Z.A. Alothman, A. Alwarthan, Recent advances in syntheses, properties and applications of TiO2 nanostructures, RSC Adv. 8 (2018) 30125–30147. https://doi.org/10.1039/c8ra06517a.

[33] F. de P. Santos, E. de Campos, M. Costa, F.C.L. Melo, R.Y. Honda, R.P. Mota, Superficial modifications in TiO2 and Al2O3 ceramics, Mater. Res. (2003). https://doi.org/10.1590/s1516-14392003000300009.

[34] M.G. Cordes, Polyvinyl alcohol, in: XPharm Compr. Pharmacol. Ref., 2011: pp. 1–2. https://doi.org/10.1016/B978-008055232-3.62444-4.

[35] T.S. Gaaz, A.B. Sulong, M.N. Akhtar, A.A.H. Kadhum, A.B. Mohamad, A.A. Al-

Amiery, D.J. McPhee, Properties and applications of polyvinyl alcohol, halloysite nanotubes and their nanocomposites, Molecules. (2015) 22833–22847. https://doi.org/10.3390/molecules201219884.

[36] J.S. Gonzalez, V.A. Alvarez, Mechanical properties of polyvinylalcohol/hydroxyapatite cryogel as potential artificial cartilage, J. Mech. Behav. Biomed. Mater. 34 (2014) 47–56. https://doi.org/10.1016/j.jmbbm.2014.01.019.

[37] E. Ozel, S. Kurama, Production of cordierite ceramic by aqueous tape casting process, J. Mater. Process. Technol. 198 (2008) 68–72. https://doi.org/10.1016/j.jmatprotec.2007.06.064.

[38] A.A. Wani, P. Singh, M.A. Shah, U. Schweiggert-Weisz, K. Gul, I.A. Wani, Rice Starch Diversity: Effects on Structural, Morphological, Thermal, and Physicochemical Properties-A Review, COMPR REV FOOD SCI F. (2012) 417–436. https://doi.org/10.1111/j.1541-4337.2012.00193.x.

[39] S. Puncha-Arnon, D. Uttapap, Rice starch vs. rice flour: Differences in their properties when modified by heat-moisture treatment, Carbohydr. Polym. 91 (2013) 85–91. https://doi.org/10.1016/j.carbpol.2012.08.006.

[40] N. Tharise, E. Julianti, M. Nurminah, Evaluation of physico-chemical and functional properties of composite flour from cassava, rice, potato, soybean and xanthan gum as alternative of wheat flour, Int. Food Res. J. 4 (2014) 573–587. https://doi.org/10.1002/fsn3.321.

[41] CES EduPack, in: Granta Des. Limited, Cambridge, UK, 2018.

[42] J. Li, S. Forberg, L. Hermansson, Evaluation of the mechanical properties of hot isostatically pressed titania and titania-calcium phosphate composites, Biomaterials. 12 (1991) 438–440. https://doi.org/10.1016/0142-9612(91)90015-3.

[43] C. Tallon, C. Chuanuwatanakul, D.E. Dunstan, G. V. Franks, Mechanical strength and damage tolerance of highly porous alumina ceramics produced from sintered particle stabilized foams, Ceram. Int. 42 (2016) 8478–8487.

https://doi.org/10.1016/j.ceramint.2016.02.069.

[44] J. Dittmann, N. Willenbacher, Micro structural investigations and mechanical properties of macro porous ceramic materials from capillary suspensions, J. Am. Ceram. Soc. 97 (2014) 3787–3792. https://doi.org/10.1111/jace.13184.

[45] U.T. Gonzenbach, A.R. Studart, E. Tervoort, L.J. Gauckler, Macroporous ceramics from particle-stabilized wet foams, J. Am. Ceram. Soc. 90 (2007) 16–22. https://doi.org/10.1111/j.1551-2916.2006.01328.x.

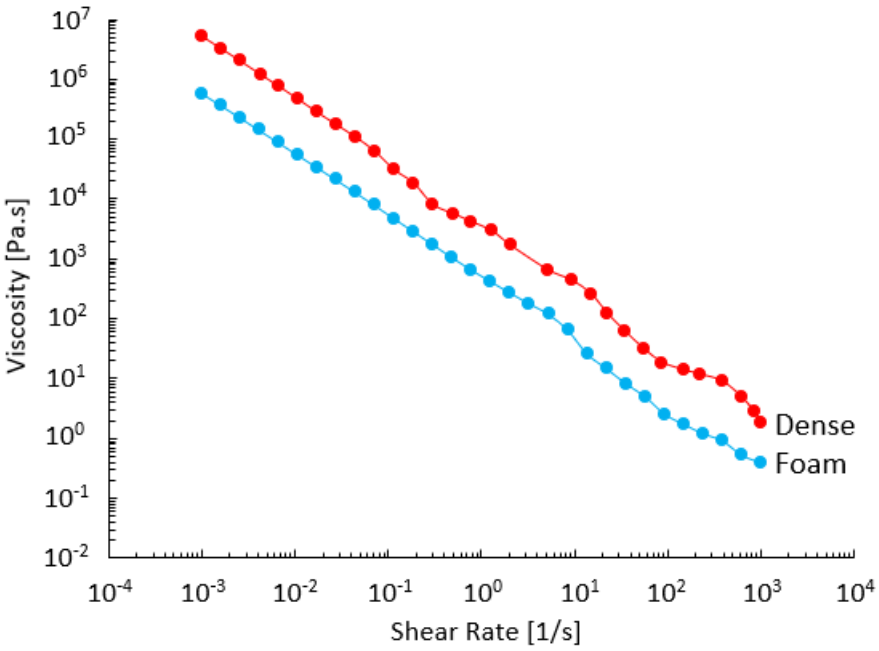

Fig. 1. Viscosity as a function of shear rate for dense and foam inks.

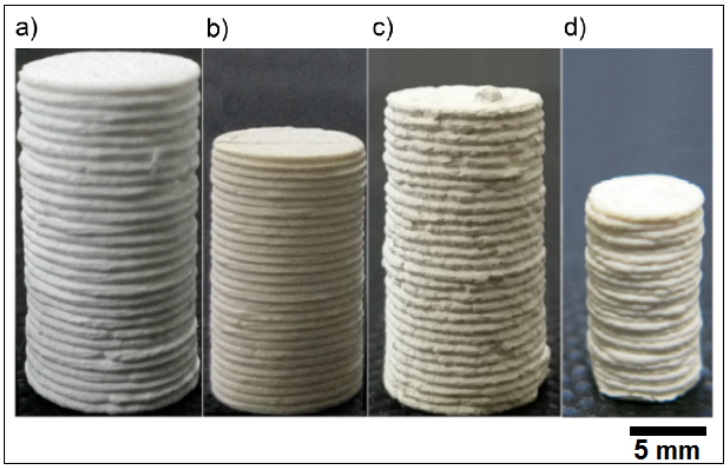

Fig. 2. Photographs of a dense sample (a) before and (b) after sintering. Likewise, a foam specimen is shown (c) before and (d) after sintering.

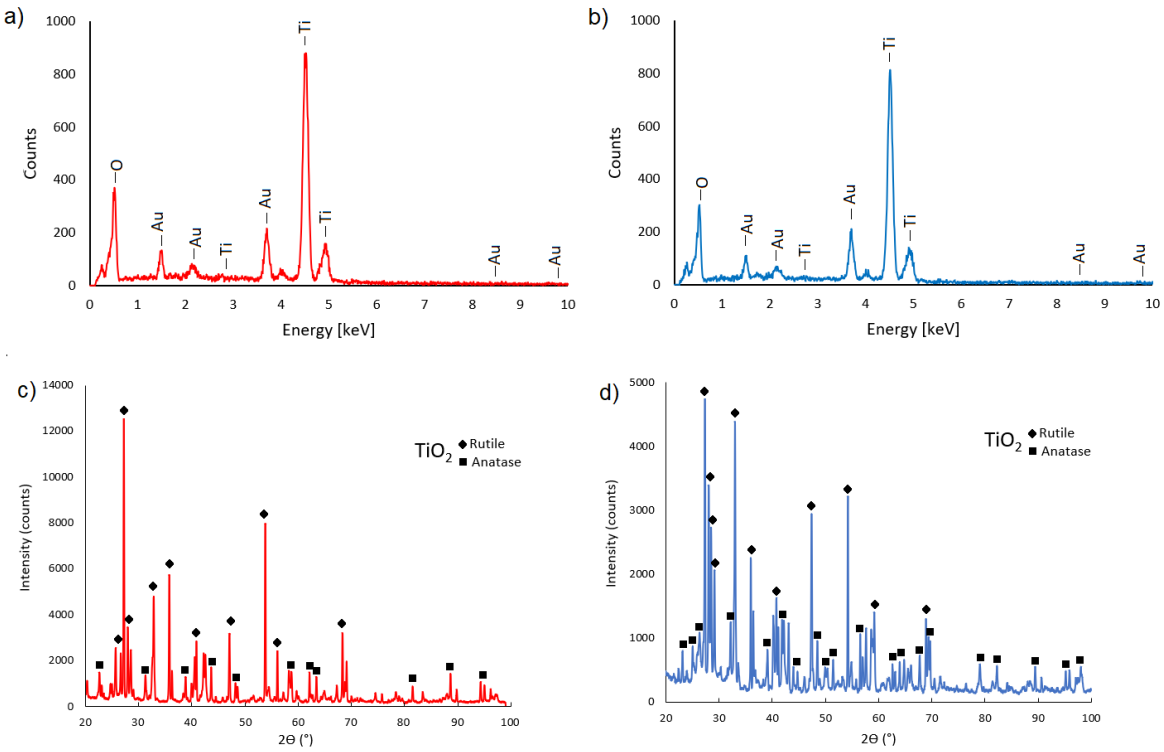

Fig. 3. EDX analysis of (a) dense and (b) foam samples. XRD analysis of (c) dense and (d) foam specimens.

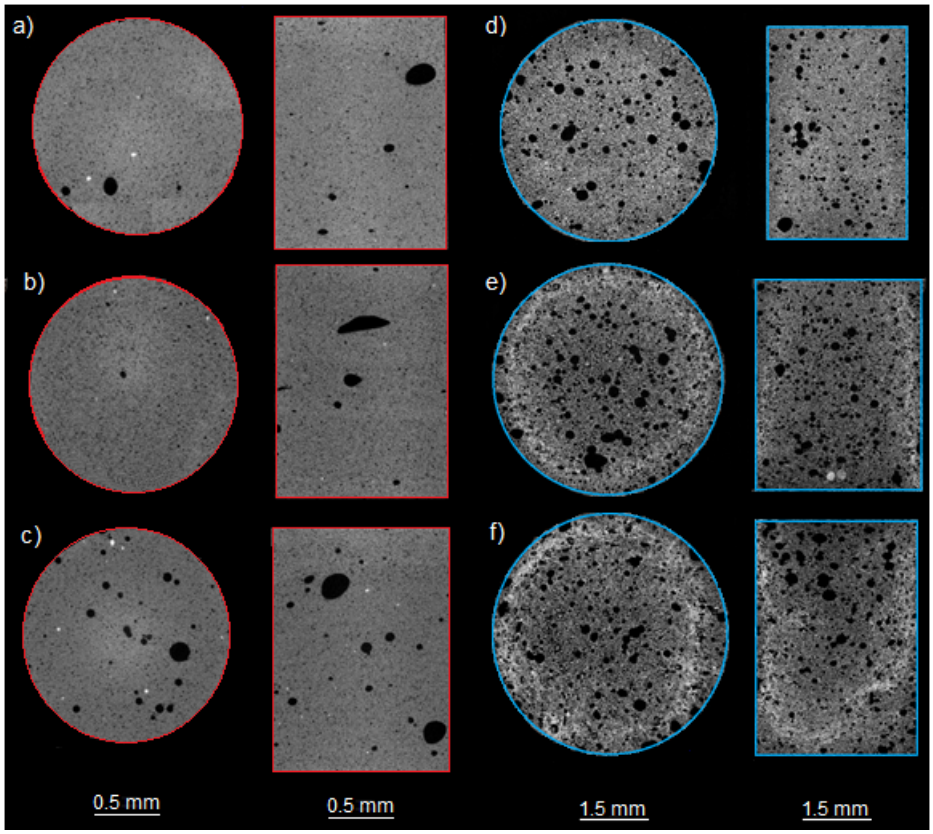

Fig. 4. Computed tomography images of dense and foam specimens. Dense samples 1, 2 and 3 are shown in parts a, b and c, respectively. Similarly, foam samples 1, 2 and 3 are shown in parts d, e and f, respectively. For each sample, the circular image is perpendicular to the longitudinal axis, whereas the rectangular image is perpendicular to the radial direction.

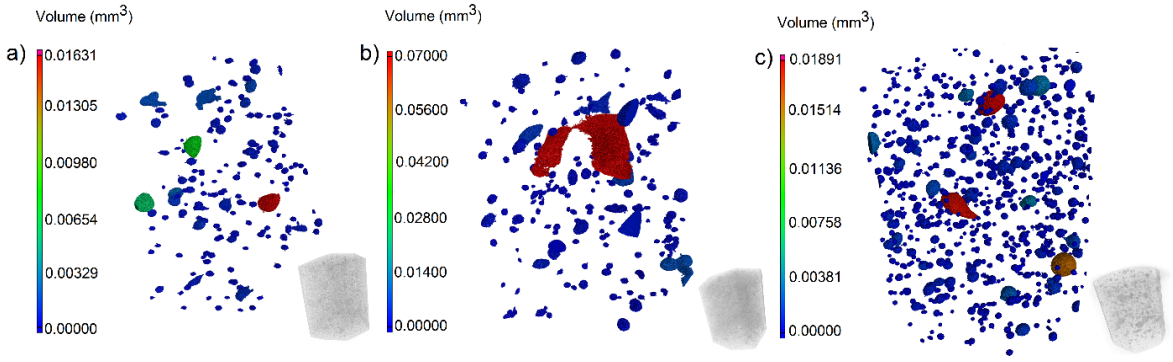

Fig. 5. Distribution and volume of the pores found in dense samples. Dense specimens 1, 2 and 3 are shown in parts a, b and c, respectively

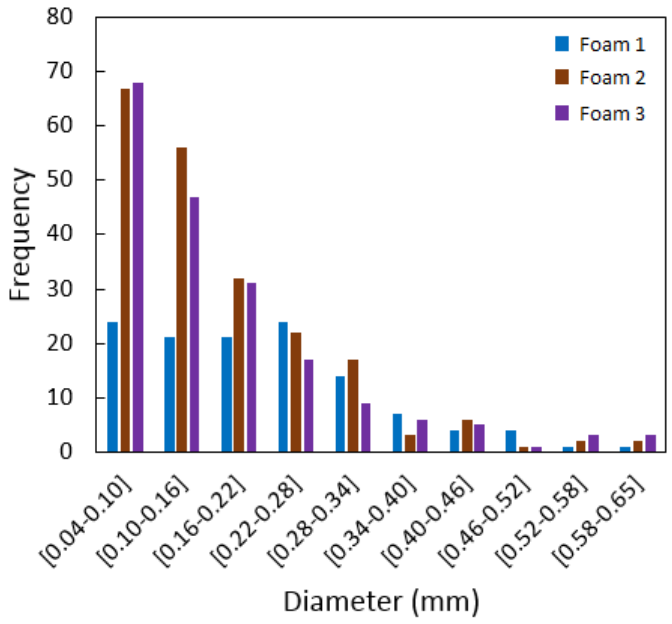

Fig. 6. Frequency distribution histogram of the pore size of foam specimens.

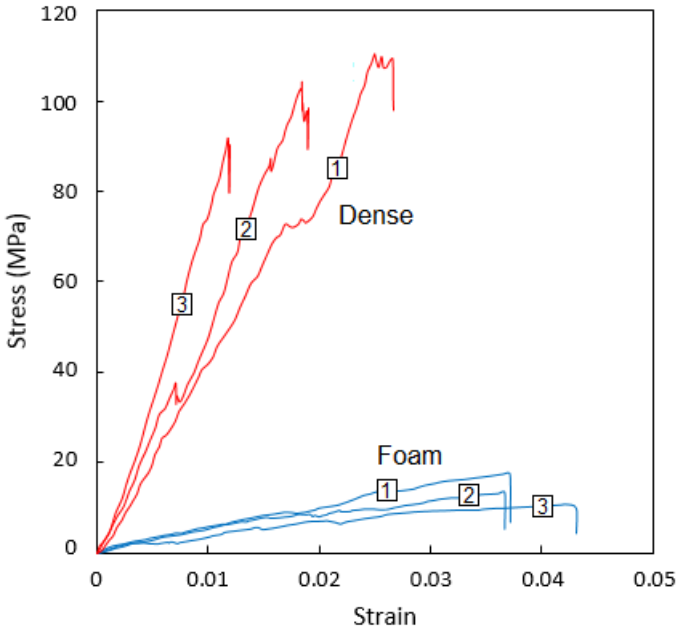

Fig. 7. Compressive stress versus strain responses measured for dense and foam specimens.

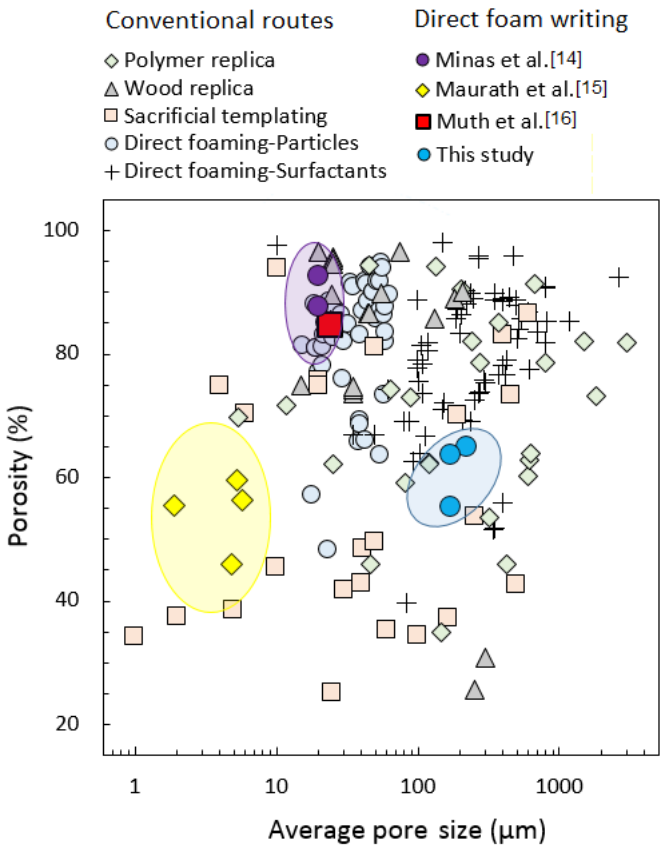

Fig. 8. Porosity and average pore size of ceramic foams produced by different manufacturing routes. Data for conventional routes come from the review of Studart et al. [6].

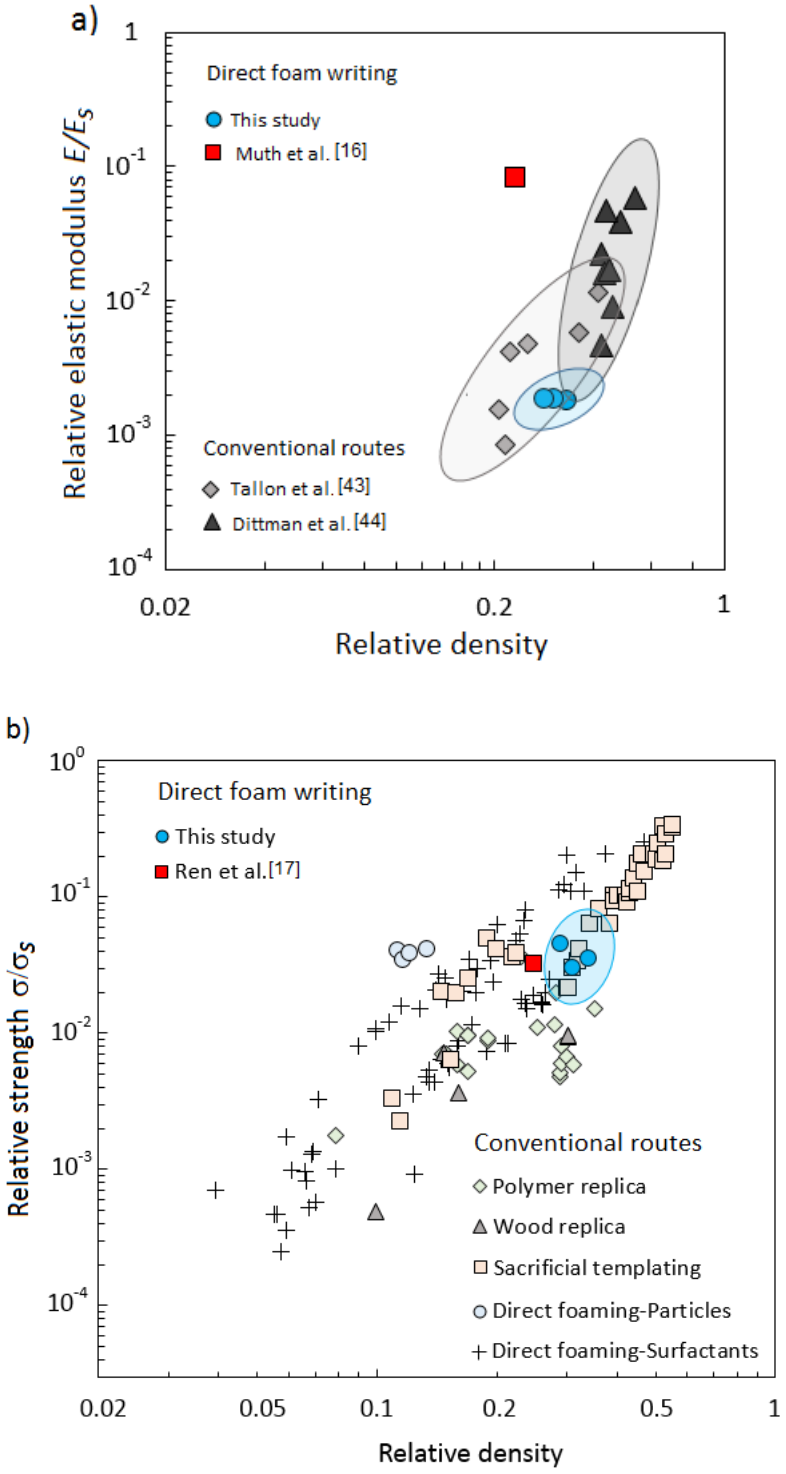

Fig. 9. Comparison between the mechanical properties of our samples and those of other ceramic foams: (a) relative elastic modulus and (b) relative compressive strength, both plotted as a function of relative density. Data for conventional manufacturing routes was collected from [43–45].

Table 1. Diameter *D* and height *H* of dense and foam samples measured after printing, drying and sintering.

Sample		Dimensions (mm)						Shrinkage (%)			
		After printing*		After drying		After sintering		After drying		After sintering	
		D	*H*	*D*	*H*	*D*	*H*	*D*	*H*	*D*	*H*
Dense	1	13.4	25.3	12.9	23.8	10.2	18.7	4	6	24	26
	2	13.6	25.0	13.0	23.9	10.2	18.4	4	4	25	26
	3	13.6	25.5	12.9	23.9	10.3	18.5	5	6	24	27
Foam	1	13.2	23.8	11.3	21.9	7.6	14.1	14	8	42	41
	2	13.2	24.0	10.9	19.5	7.4	14.0	17	19	44	42
	3	13.0	23.3	10.5	17.6	7.0	11.7	19	24	46	50

Table 2. Physical and mechanical properties of dense and foam samples.

Sample		Mass (g)	Density (g/cm^3)	Porosity (%)	Elastic modulus (GPa)	Strength (MPa)
Dense	1	5.55	3.60	8.6	6.3	112
	2	5.24	3.48	13.1	5.0	104
	3	5.06	3.32	17.6	4.0	92
Foam	1	0.79	1.22	63.7	0.48	14
	2	0.65	1.08	65.0	0.50	12
	3	0.57	1.03	55.1	0.50	18